Biosensors and Bioelectronics 167 (2020) 112505

Contents lists available at ScienceDirect

Biosensors and Bioelectronics

journal homepage: http://www.elsevier.com/locate/bios

Multiplexed femtomolar detection of Alzheimer's disease biomarkers in biofluids using a reduced graphene oxide field-effect transistor

Dongsung Park [a,b,1], Jae Hyun Kim [a,1], Hye Jin Kim [a], Dongtak Lee [b], David S. Lee [a], Dae Sung Yoon [b,*], Kyo Seon Hwang [a,**]

[a] Department of Clinical Pharmacology and Therapeutics, College of Medicine, Kyung Hee University, Seoul, 02453, Republic of Korea
[b] School of Biomedical Engineering, Korea University, Seoul, 02841, Republic of Korea

ARTICLE INFO

Keywords:
Reduced graphene oxide field-effect transistor
Multiplexed detection
Alzheimer's disease
Amyloid-β
Tau protein

ABSTRACT

Alzheimer's disease (AD) is a neurodegenerative disease that accounts for 70% of all dementia. Early stage diagnosis of AD is essential as there is no certain treatment after the lesion has progressed in the late stage. Nevertheless, there are still limitations of early diagnosis of AD using neuroimaging and psychological memory assessments. Here, we demonstrate ultrasensitive and multiplexed detection of pivotal AD biomarkers ($A\beta_{1\text{-}42}$ and t-Tau) in biofluids using a reduced graphene oxide field-effect transistor (gFET). The proposed approach provides a wide logarithmically linear range of detection from 10^{-1}–10^{5} pg mL^{-1} and a femtomolar-level limit of detection in biofluids (human plasma and artificial cerebrospinal fluid) as well as phosphate-buffered saline (PBS). Furthermore, as these core biomarkers have different surface charges in physiological conditions based on the isoelectric point (pI), we achieved a distinctive output signal for each biomarker. The gFET biosensor platform presented in this paper has great potential and can be used for early diagnosis of AD in clinical practice as well as accurate analysis based on the surface charge of the analytes.

1. Introduction

To accurately diagnose Alzheimer's disease (AD) at its predementia stage would be a major breakthrough from therapeutic and prevention standpoints (Sügis et al., 2019). Recently, there has been a major paradigm shift from major hallmarks (e.g., amyloid-beta plaques and neurofibrillary tangles) to biomarker detection in cerebrospinal fluid (CSF). Specifically, the modified AD biomarker-based diagnostic criteria include A, T, and N classification systems, which refer to concentrations of amyloid-β (Aβ), tau protein, and neurodegeneration biomarkers, respectively (Lee et al., 2019). Among these biomarkers, Aβ and tau protein play pivotal role in early diagnosis of AD (Parnetti et al., 2019), as they are related to the initial progress of AD (Nisbet et al., 2015). Moreover, Park et al. reported that the ratio of the concentration of tau protein in plasma to that of Aβ has a high correlation with neurodegeneration in AD patients (Park et al., 2019). Chen et al. recently reported that plasma $A\beta_{1\text{-}42}$ and total-tau (t-Tau) levels may predict amnestic mild cognitive impairment (MCI) (aT. Bin Chen et al., 2019). As the combined analysis of biomarkers such as tau protein and Aβ rather than single biomarkers becomes increasingly important in diagnosis(Janelidze et al., 2020), the demand for multiplex detection platforms in body fluids for these biomarkers is increasing.

Enzyme-linked immunosorbent assay (ELISA) is one of the most common analytical technique used to measure the concentration of AD biomarkers (Verwey et al., 2009). However, this does not sufficiently satisfy the limit of detection (LOD) or sensitivity of biomarkers present in a few picograms of body fluids particularly serum or plasma. To address the limitations of conventional methods, various studies have been conducted to detect AD biomarkers such as electrochemical (Hassan and Kerman, 2019), optical (Carrico et al., 2017), and impedimetric (Ngoc Le et al., 2019) methods. Among these methods, field-effect transistor (FET) biosensors have attracted increased attention for a label-free detection of biomolecules owing to their excellent sensitivity, selectivity, and sub-picomolar LOD (Kaisti, 2017). A graphene-based FET (gFET) biosensor is considered one of the most promising biosensors, as graphene possesses extremely high

* Corresponding author.
** Corresponding author.
E-mail addresses: dsyoon@korea.ac.kr (D.S. Yoon), k.hwang@khu.ac.kr (K.S. Hwang).
[1] D. Park and J. H. Kim contributed equally to this work.

https://doi.org/10.1016/j.bios.2020.112505
Received 11 May 2020; Received in revised form 31 July 2020; Accepted 7 August 2020
Available online 15 August 2020

charge-carrier mobility and chemical robustness (Fu et al., 2017). In addition, a two-dimensional (2D) gFET channel provides numerous binding sites for immobilization of receptors compared with a one-dimensional based FET such as silicon nanowire or carbon nanotube. Chen et al. reported an aptamer-based gFET to detect tobramycin with sub-nanomolar detection within a few seconds (bX. Chen et al., 2019). Furthermore, Wu et al. recently developed a dual-aptamer based gFET to detect hepatocellular carcinoma-derived micro-vesicles (Wu et al., 2020).

Apart from aptamer, various bio-receptors have been used for label-free detection of biomolecules. Zhang et al. reported photocatalytic renewable gFET biosensors for the detection of highly sensitive D-dimer (Zhang et al., 2016). Yu et al. successfully developed gFETs for quantitative detection of exosomes derived from prostate cancer using exosome-specific CD63 antibodies (Yu et al., 2019). Lei et al. reported brain natriuretic peptide (BNP) detection with platinum nanoparticles (PtNPs)-decorated gFET from whole blood (Lei et al., 2017). These solution-gated gFETs mainly depend on the electrostatic gating effect generated by the conformational change of aptamer (i.e. G-quadruplex) or the surface charge density of analytes (Hao et al., 2017). In the case of protein analytes, the surface charge density is determined by the pI value of each analyte, and the gFETs can interpret the target analyte by measuring the doping effect produced by binding the target analyte to receptors. However, gFETs that can facilitate multiplexed detection of two highly related biomarkers possessing different electrical properties have not yet been reported.

In this paper, we describe a highly sensitive gFET sensor for simultaneous multiplexed detection of $A\beta_{1\text{-}42}$ and t-Tau, which have different electrical properties in physiological fluids as depicted in Fig. 1. Specifically, $A\beta_{1\text{-}42}$ is negatively charged in physiological conditions, which induces n-doping effect on a gFET sensor. In contrast, t-Tau is positively charged in physiological fluids, which induces p-doping effect on a gFET sensor. We developed a gFET platform for multiplexed femtomolar detection of $A\beta_{1\text{-}42}$ and t-Tau using these mechanisms. This platform enables AD biomarker detection in various physiological solutions (i.e., PBS buffer, plasma, aCSF) within several minutes. The proposed charge-based approach represents a useful and universal gFET biosensing strategy for multiplexed detection of protein biomarkers and related clinical diagnosis.

2. Experimental

2.1. Fabrication of the graphene-based FET biosensor

First, a 300-nm silicon dioxide (SiO_2) layer was grown by thermal oxidation on 4-in p-type silicon wafers. The SiO_2 substrates were cleaned using a piranha solution (H_2SO_4: H_2O_2 = 3:1) for 30 min to activate the surface with high density hydroxyl functional groups. The cleaned substrates were then reacted in 1% 3-(ethoxydimethylsilyl)propylamine (APMES, Sigma-Aldrich, Republic of Korea) diluted in ethanol for 1 h to form amine functional groups (-NH2). The APMES-treated substrates interact with GO flakes through electrostatic interaction. A GO solution was produced using the modified Hummers' method and dispersed in distilled water (DW). This aqueous GO solution was spin-coated on the APMES-treated SiO_2 substrate at 500 rpm for 5 s and 3000 rpm for 60 s. Strong adhesion was achieved between GO flakes and substrates by electrostatic interaction between the amine group ($-NH_2$) derived from the APMES self-assembly monolayer (SAM) and carboxyl groups on the GO flakes. Finally, to obtain reduced graphene oxide (rGO) films, the GO thin films were chemically reduced using hydroiodic acid (HI, Sigma-Aldrich, Republic of Korea) vapor at 80 °C for 3 h.

The rGO thin films were patterned via photolithography and reactive ion etching (RIE) to achieve dimensions of 40 μm × 80 μm (width × length). For each process, a lift-off resist layer (LOR 10B, MicroChem, USA) was spin-coated under the patterning photoresist (PR) layer to reduce the PR residue. The drain and source electrodes (Ti/Au = 5 nm/60 nm) were fabricated using e-beam evaporation and bilayer lift-off techniques. Finally, the patterned electrodes were passivated using a chemically stable SU-8 photoresist (SU-8 2002, MicroChem, USA), and the rGO active layer was partially opened.

2.2. Surface functionalization

The rGO patterned devices were soaked in 50-mM 1-pyrenebutyric acid N-hydroxysuccinimide ester (PBASE, Sigma-Aldrich, Republic of Korea) diluted in dimethyl sulfoxide (DMSO, Sigma-Aldrich, Republic of

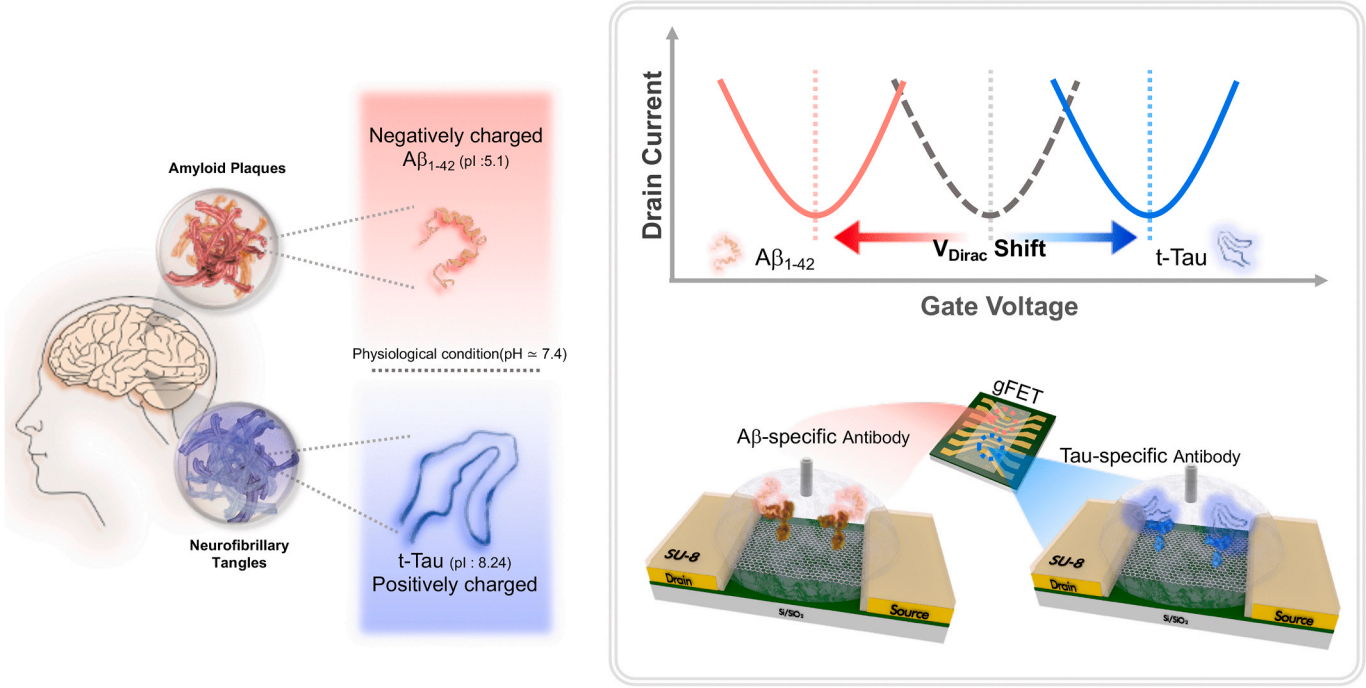

Fig. 1. Schematic illustration of the graphene-based field-effect transistor (gFET) for multiplex detection of $A\beta_{1\text{-}42}$ and t-Tau.

Korea) for 2 h at 25 °C to immobilize the antibodies. After incubation, the devices were washed with pure DMSO, ethanol, and DW. The pyrene group on one end of PBASE was adsorbed on the surface of the rGO through π–π stacking interactions, and the succinimidyl ester group on the other end reacted with the amine group on the antibodies. Anti-Aβ monoclonal antibody (6E10, BioLegend, UK) and anti-Tau monoclonal antibody (Tau-5, Thermo Fisher Scientific, Republic of Korea) were prepared at a concentration of 10 μg/mL in a 10-mM phosphate buffer (PB) (pH 7.4) and incubated for 2 h on PBASE-modified rGO channels at room temperature (RT). Finally, we treated 100 mM of ethanolamine (Sigma-Aldrich, USA) diluted in 10 mM of PB for 1 h at RT. Ethanolamine was used as a blocking agent for the unreacted aldehyde groups on PBASE to prevent non-specific adsorption. The zeta-potential of both 6E10 and Tau-5 antibodies were measured by a particle size analyzer (Zetasizer Nano-ZS90, Malvern, UK).

2.3. Device characterization and electrical measurement

A semiconductor parameter analyzer (KEITHLEY 4200A-SCS, USA) and a customized Faraday cage (FRD, Republic of Korea) were used to measure the electrical properties of fabricated rGO devices. A customized micro-channel embedded jig, composed of polyimide (PI), polycarbonate (PC), and polyether ether ketone (PEEK), was fabricated to fix the leakage-free Ag/AgCl reference electrode (LF-2, Harvard Apparatus) and the rGO device. To profile the surface of the rGO channel, we used atomic force microscopy (AFM, NX 10, Park Systems, Republic of Korea) and X-ray photoelectron spectroscopy (XPS, K-Alpha, Thermo Fisher Scientific, USA). XPS spectra of GO and rGO thin film are shown in Figs. S1A, B, and C.

$A\beta_{1\text{-}42}$ (Tocris Bioscience, UK) and t-Tau (Abcam plc, UK) were spiked into PBS, artificial CSF (aCSF) (Tocris Bioscience, UK), and human plasma (Sigma-Aldrich, Republic of Korea) at various concentrations. Since $A\beta_{1\text{-}42}$ is prone to aggregation, $A\beta_{1\text{-}42}$ peptides were prepared in the same way as described in our previous paper (Yoo et al., 2020). Then, 20 μL of a peptide-spiked solution was injected into the 6E10 and Tau-5 immobilized devices from low to high concentration, respectively. After 30 min of incubation of peptide-spiked solutions (PBS, aCSF, and human plasma), the devices were washed with a 10-μM PBS solution. Measurements of the rGO transfer curves were performed under a 10-μM PBS environment without buffer flow, which was selected considering the Debye length of the PBS solution (Nakatsuka et al., 2018). Fig. S3A demonstrates the ionic dependence on Debye lengths and the size of IgG antibody. In addition, we measured the antibody–antigen response by serial concentrations in a 10 mM PBS environment and could see that the transfer curve of the gFET barely changed (Figs. S3B, S3C and S3D).

3. Results and discussion

3.1. Device characterization

Organic contamination on the rGO surface due to PR residue can lead to considerable device malfunctions. To prevent PR contamination, several studies have employed thin oxide or nitride layer deposition for sacrificial layers on 2D-material surfaces (Chae et al., 2018). However, these processes require additional deposition and etching steps that can damage the active channel layer. Therefore, we coated a lift-off resist (LOR 10B) layer under the patterning PR layer during rGO channel fabrication. In Figs. S1D and E, the difference between cases with and without LOR 10B are shown. AFM images indicate that the PR residues remained not only immediately after the fabrication but also after washing in acetone for 2 h. Compared with the method where the patterning PR is in direct contact with the rGO surface, the roughness of the fabricated rGO surface using LOR 10B decreased from 1.5 nm to 0.9 nm. The thickness of the fabricated rGO channel was measured as 9.06 ± 0.38 nm through AFM analysis.

Electrical characterization of the fabricated devices was performed prior to the specific detection of proteins. Each FET device was composed of six isolated rGO channels, and the length of the exposed channel was 10 μm. In Fig. 2A, a single FET device and an optical microscope image of a fabricated channel are depicted. Fig. 2B shows the schematic and cross-sectional illustrations of our customized jig system. To assess the chip-to-chip resistance deviation of the rGO sensors, we selected five chips on a single wafer. The measured average resistances of the sensors (chips 1–5) were 1.288 ± 0.122 kΩ, 1.299 ± 0.149 kΩ, 1.249 ± 0.107 kΩ, 1.261 ± 0.167 kΩ, and 1.260 ± 0.072 kΩ, respectively (Fig. 2C). The chip-to-chip resistance variation was 1.6%, which indicates that the devices were fabricated correctly with high uniformity. The I_{ds}–V_{ds} output curves of the rGO-FET device in an aqueous environment obtained by varying the gate voltage (V_g) in the range of 0–1.5 V with a low V_{ds} range are shown in Fig. 2D. The high linearity of the output curve indicates good ohmic contact between the sensing channel and electrodes. In Fig. 2E, a plot of the transfer curves (I_{ds}–V_g) obtained by sweeping V_g from −1.0 V to 1.0 V at various V_{ds} values in the range of 100–150 mV is shown. It demonstrates the intrinsic ambipolar characteristics around the Dirac point (V_{Dirac}) of the rGO channels. Furthermore, we measured the leakage current from Ag/AgCl reference electrode. As shown in Fig. S2B, the magnitudes of leakage currents were very small (several nA) compared to that of the source–drain current (~50 μA), indicating that the fabricated gFETs were thoroughly passivated.

For a specific antigen detection, the rGO surfaces were functionalized with PBASE, followed by a covalent immobilization of antibody reaction. A schematic diagram of the antibody immobilization process is shown in Fig. 3A. AFM images before and after antibody immobilization reveal that the antibodies were effectively immobilized to the functionalized surface (Fig. 3D and G). Roughness measurements of the bare rGO surface and the surface after antibody immobilization show that the roughness of the surface area (R_a) increased from 0.93 nm to 1.34 nm. Electrical characterization was also performed for each step of the antibody immobilization process. The characteristic ambipolar transfer curves for each step of anti-Aβ antibody (6E10) immobilization and the V_{Dirac} distribution of corresponding steps are shown in Fig. 3B and D. Similarly, in Fig. 3C and F, the characteristic curves of the stepwise functionalization process of Tau-5 are shown.

The Dirac point of the fabricated rGO-FET devices was approximately 55.76 ± 16.37 mV. The functionalization of PBASE to the rGO surface increased V_{Dirac} from 55.76 ± 16.37 mV to 240.9 ± 62.99 mV, which shows that PBASE provides strong p-type doping in rGO (Yue et al., 2017; Jin et al., 2019). The zeta potential of 6E10 and Tau-5 antibodies were observed to be approximately −13.9 mV and −15.5 mV, respectively, in 10 mM PBS (pH 7.4) (Fig. S2A). As both 6E10 and Tau-5 antibodies are negatively charged in PBS, the transfer characteristic curves were left-shifted because of n-doping effect of antibodies. After 6E10 and Tau-5 were immobilized on rGO surface, their V_{Dirac} values decreased from 248.1 ± 52.1 mV to 139.2 ± 13.1 mV and 233.0 ± 39.0 mV to 125.9 ± 24.3 mV, respectively. After ethanolamine blocking, the Dirac points of 6E10-immobilized gFET and Tau5-immobilized gFET were shifted from 139.2 ± 13.1 to 150.64 ± 48.14 and 125.9 ± 24.3 to 151.34 ± 73.29, respectively. In the same context, when the antigens bind to their specific antibodies, the net carrier density on the rGO surface varies owing to the contributions of the electrical charges of $A\beta_{1\text{-}42}$ and t-Tau in the buffer solution (Kim et al., 2013).

3.2. Specific detection of the target proteins in PBS solution

Prior to AD detection in biofluids, the fabricated rGO devices were analyzed to determine their capabilities for specific protein detection in a PBS buffer solution. $A\beta_{1\text{-}42}$ and t-Tau are known as the hallmarks of AD and are composed of 42 and 441 amino acids, respectively. The pI value, the pH at which a protein (molecule) has a neutral charge, of $A\beta_{1\text{-}42}$ is

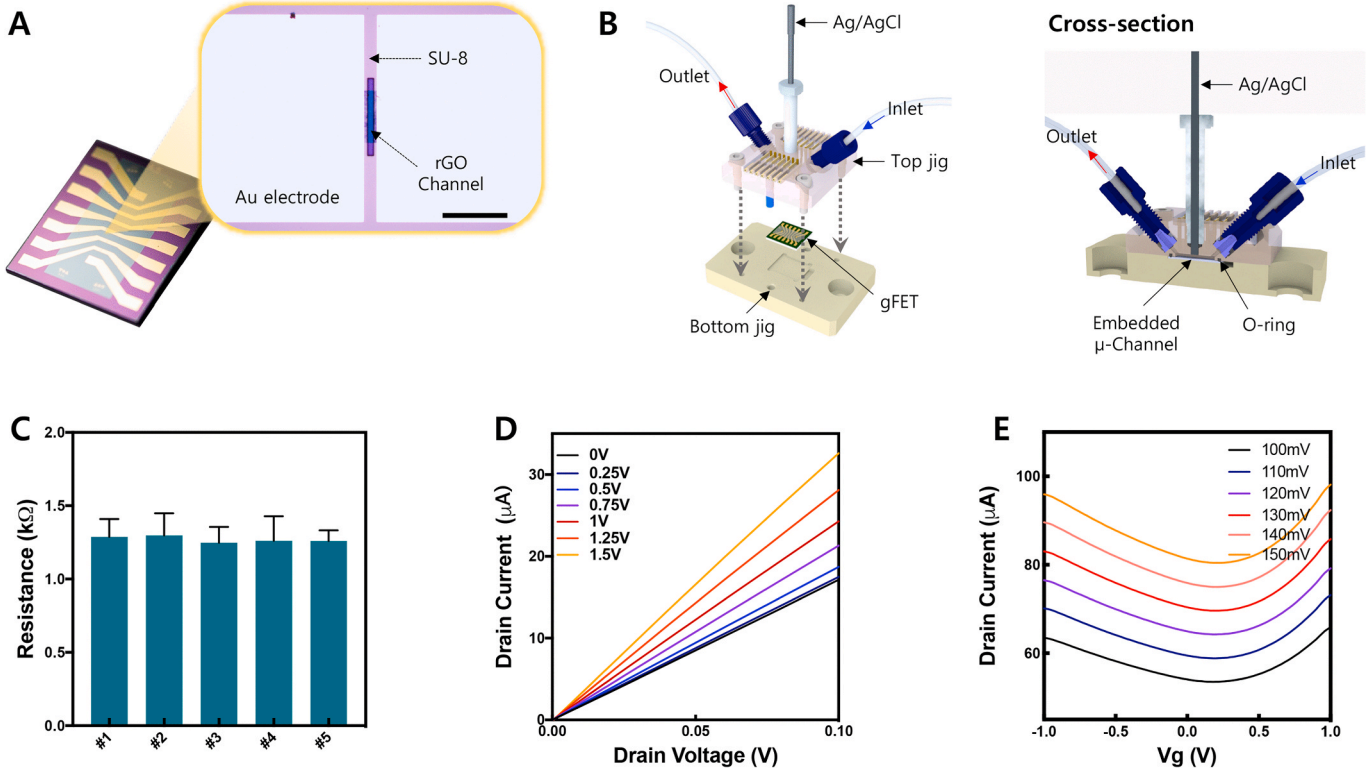

Fig. 2. Device characterization and measurement configuration. (A) The photograph and optical images of gFET. The scale bar in optical image indicate 100 μm. (B) The front and cross-section view that shows the composition of a customized jig with gFET and Ag/AgCl reference electrode. (C) The chip-to-chip resistance deviation of the rGO sensors. Error bars correspond to standard deviations (n = 5). (D) Typical output characteristic (I_{ds}–V_g) with varying V_g from 0 V to 1.5 V. (E) Ambipolar transfer characteristic of gFET. V_{ds} is varied from 100 mV to 150 mV.

approximately 5.1 (Janas et al., 2019), which indicates that A$\beta_{1\text{-}42}$ is negatively charged in the PBS solution (pH = 7.4). Furthermore, the accumulation of A$\beta_{1\text{-}42}$ induces an increase in the net carrier density, which leads to n-doping on the rGO channel with a left shift of the graphene transfer curves. As the concentration of A$\beta_{1\text{-}42}$ increased from 100 fg/mL to 100 ng/mL, n-doping occurred on the surface of the rGO channel, and the Dirac point of the transfer curve shifted to the left (Fig. 4A). In Fig. 4B, the ΔV_{Dirac} values of gFETs were measured as −21.68 ± 4.00 mV, −28.25 ± 3.28 mV, −38.79 ± 4.77 mV, −55.05 ± 0.60 mV, −70.78 ± 6.14 mV, −88.29 ± 3.34 mV, and −104.80 ± 1.56 mV with A$\beta_{1\text{-}42}$ concentrations of 100 fg/mL, 1 pg/mL, 10 pg/mL, 100 pg/mL, 1 ng/mL, 10 ng/mL, and 100 ng/mL, respectively. ΔV_{Dirac} means the change in the Dirac point, which is formulated as $\Delta V_{dirac} = V_{dirac,\ before\ incubation} - V_{dirac,\ after\ incubation}$. The ΔV_{Dirac} of 100 fg/mL A$\beta_{1\text{-}42}$ exceeded that of the noise level, indicating that the gFET could detect up to 100 fg/mL of A$\beta_{1\text{-}42}$ with a high sensitivity. To set the noise level, the PBS blank control test was conducted four times, and ΔV_{Dirac} values were 1.61 mV, −3.26 mV, 1.09 mV, and 1.85 mV (Fig. S3E). From this result, since the standard deviation was calculated as 2.09 mV, the LOD was determined to be 6.27 mV, which is three times the standard deviation. The dashed line represents the signal/noise ratio of 3 from PBS blank control test. Furthermore, a linear relationship was obtained between A$\beta_{1\text{-}42}$ concentration and ΔV_{Dirac} from 1 pg/mL to 100 ng/mL A$\beta_{1\text{-}42}$, which is a clinically reasonable range to diagnose AD (Song et al., 2011). A linear regression equation of the response was obtained as $\Delta V_{Dirac} = -15.63 \log C - 25.26$, with a correlation coefficient (R^2) of 0.995, where C is the A$\beta_{1\text{-}42}$ concentration.

In contrast, t-Tau has a pI value of approximately 8.24 (Weickert et al., 2020), resulting in a decrease in the net carrier density owing to binding of t-Tau to Tau-5 antibody. Finally, the transfer curve shifted to the right, indicating that p-doping occurred on the rGO channels as the concentration of t-Tau gradually increased (Fig. 4D). The ΔV_{Dirac} values of gFETs were measured as 33.74 ± 1.18 mV, 55.18 ± 2.40 mV, 77.29 ± 5.12 mV, 103.44 ± 8.47 mV, 124.42 ± 3.69 mV, 133.79 ± 0.12 mV, and 148.53 ± 5.94 mV for a series of t-Tau concentrations from 100 fg/mL to 100 ng/mL. These data are plotted in Fig. 4E, where the dashed line represents the signal/noise ratio of 3 obtained from the PBS blank control test. In terms of t-Tau detection, a linear relationship was obtained between t-Tau concentration and ΔV_{Dirac} from 100 fg/mL to 1 ng/mL concentration, which also represents a clinically reasonable range to diagnose AD (Pillai et al., 2019). A regression equation of the response was formulated as $\Delta V_{Dirac} = 22.96 \log C + 55.85$, with a correlation coefficient (R^2) of 0.999, where C is the t-Tau concentration. These results indicate that the study achieved high sensitivity and dynamic range of gFET for specific detection in biofluids.

3.3. Specificity and multiplex detection of the biosensor

To verify the specificity of gFET biosensors, we investigated various concentrations of non-specific controls. The crosstalk between t-Tau to anti-Aβ antibody and A$\beta_{1\text{-}42}$ to anti-t-Tau was measured and the results are shown in Figs. S4A and S4D. In terms of the 6E10-immobilized gFET, 10 pg/mL, 1 ng/mL, and 100 ng/mL of t-Tau were incubated serially. Similarly, 10 pg/mL, 1 ng/mL, and 100 ng/mL of A$\beta_{1\text{-}42}$ were injected on the Tau-5-immobilized sensors. As shown in Figs. S4A and S4D, a minimal shift in the I_{ds}–V_g transfer curve was observed regardless of the concentrations of non-specific targets. The ΔV_{Dirac} of 10 pg/mL, 1 ng/mL, and 100 ng/mL t-Tau on 6E10-immobilized were 3.48 mV, 5.48 mV, and 8.21 mV, respectively. In the case of Tau-5 immobilized gFET, the ΔV_{Dirac} of 10 pg/mL, 1 ng/mL, and 100 ng/mL A$\beta_{1\text{-}42}$ were −1.85 mV, −2.58 mV, and −5.17 mV, respectively. The crosstalk between t-Tau to anti-Aβ antibody and A$\beta_{1\text{-}42}$ to anti-t-Tau was less than the noise level. This indicates that there was no significant non-specific adsorption on each antibody-immobilized surface. Furthermore, 10 pg/mL, 1 ng/mL,

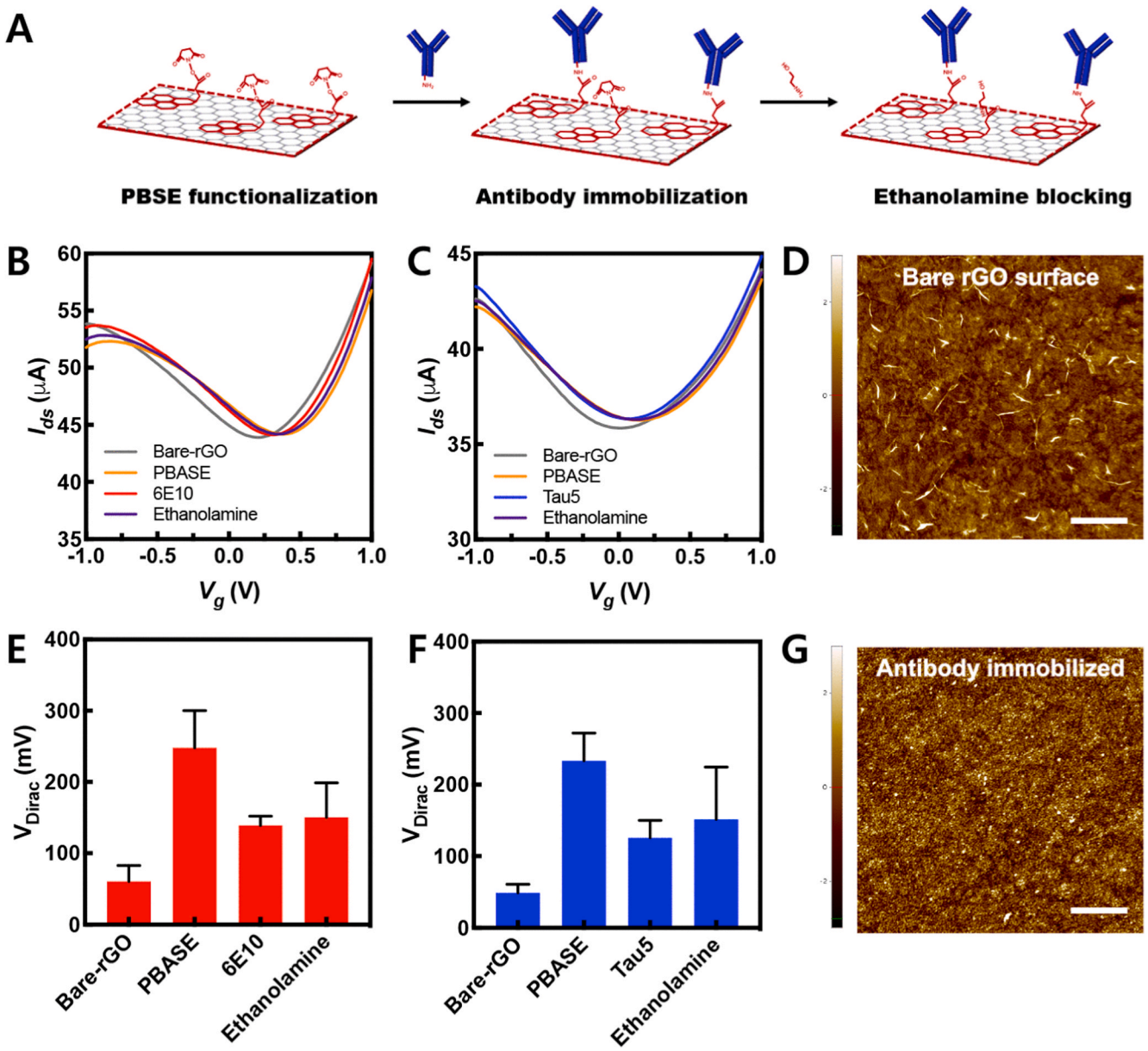

Fig. 3. Characterization of antibody immobilization of gFET. (A) Schematic illustration of antibody immobilization procedure on rGO surface. (B) Transfer characteristics and (E) variation in V_{Dirac} of bare-rGO surface, PBASE modification, Aβ-specific antibody (6E10) immobilization, and ethanolamine blocking. (C) Transfer characteristics and (F) variation in V_{Dirac} of surface modification and immobilization of Tau-specific antibody (Tau-5). Error bars represent standard deviations (n = 5). Topological analysis of (D) bare and (G) antibody-immobilized rGO surface (scale bar: 1 μm).

and 100 ng/mL of the brain-derived neurotrophic factor (BDNF) were tested as another non-specific target of both 6E10 and Tau-5-immobilized gFETs (Figs. S4B and S4E). The ΔV_{Dirac} of 10 pg/mL, 1 ng/mL, and 100 ng/mL BDNF were 5.40 mV, 5.13 mV, and 8.74 mV on 6E10-immobilized channels, and 4.67 mV, 4.59 mV, and 7.12 mV on Tau-5-immobilized channels, respectively. In contrast, the ΔV_{Dirac} of 10 pg/mL, 1 ng/mL, and 100 ng/mL $A\beta_{1\text{-}42}$ on 6E10-immobilized gFETs, the specific antigen-antibody, were −38.79 mV, −70.78 mV, and −104.80 mV, respectively. Similarly, the ΔV_{Dirac} of 10 pg/mL, 1 ng/mL, and 100 ng/mL t-Tau on Tau-5-immobilized gFETs were 77.29 mV, 124.42 mV, and 148.53 mV, respectively. The specific targets, $A\beta_{1\text{-}42}$ and t-Tau, both exhibited significantly greater ΔV_{Dirac} than the non-specific target or blank control in specific reactions, and the results are summarized in Figs. S4C and S4D. These results indicate that both 6E10 and Tau-5-immobilized gFETs have outstanding specificity and great potential for use in a multiplex detection platform.

Moreover, we conducted a complex specificity test to clarify the detection capacity of gFET by incubating other neurodegenerative disease biomarkers and their mixtures. The candidates for non-specific control were determined by considering the pathological factor of biomarkers as well as the pI value. In considering these points, we determined alpha-synuclein (α-syn) and BDNF as factors in the complex specificity test. α-syn is an amyloid protein associated with dementia with Lewy bodies, Parkinson's disease, as well as AD, and it is known to have a pI value of 4.67 (Mor et al., 2016; Shahnawaz et al., 2020). Therefore, α-syn is negatively charged at pH of 7.4 owing to its pI value. In contrast, BDNF is a biomarker associated with AD and depression (Tsai, 2003), and it has a positive charge in a physiological environment because its pI value is in the range of 9–10 (Hempstead, 2015).

The transfer curves obtained from sequential reactions with 10 pg/mL of BDNF, t-Tau, α-syn, and $A\beta_{1\text{-}42}$ to 6E10-immobilized gFET are shown in Fig. S5A. The ΔV_{Dirac} of non-specific proteins (BDNF, t-Tau,

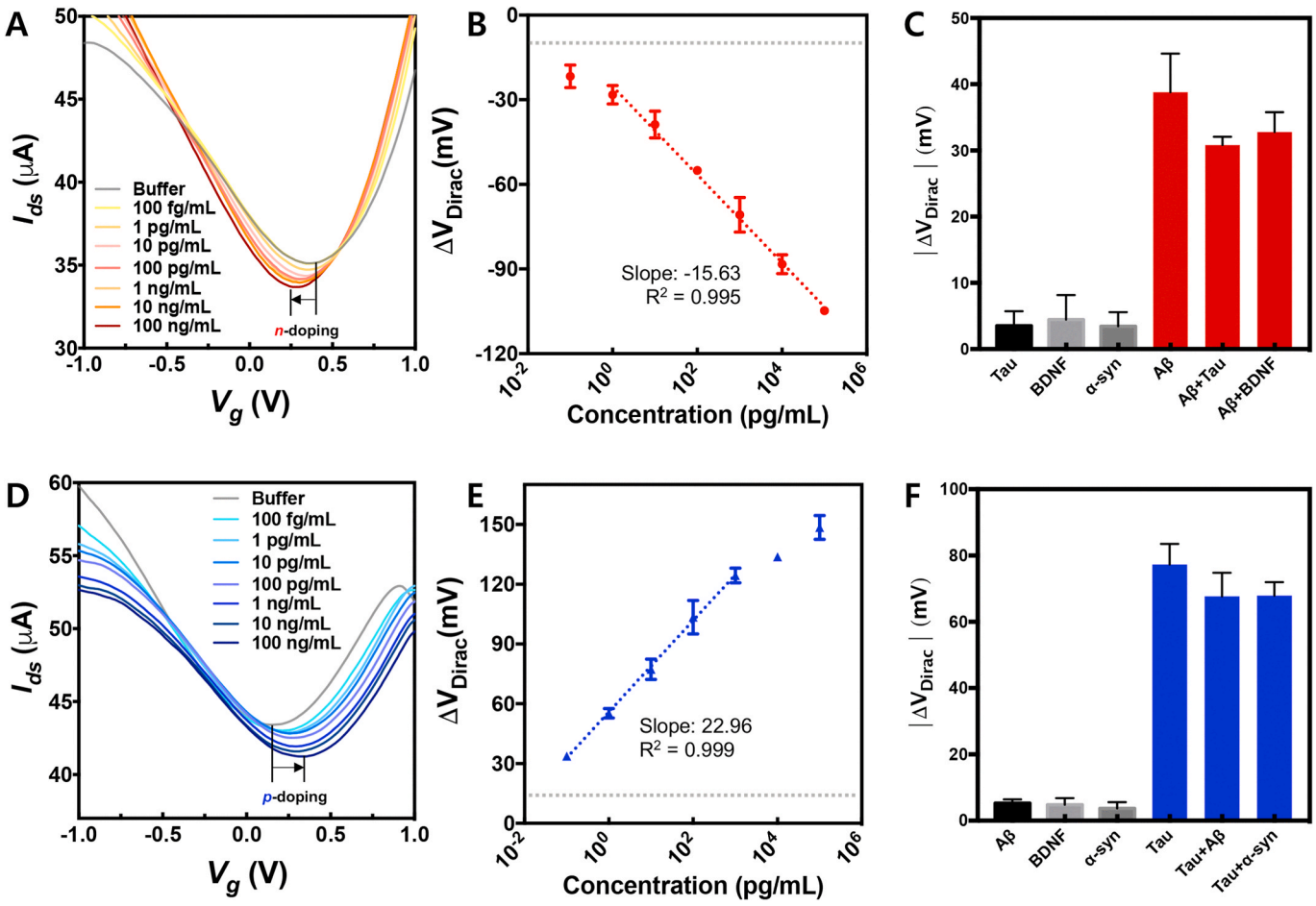

Fig. 4. (A) Transfer curves and (B) the shift of V_{Dirac} of the 6E10-immobilized gFET biosensor that interacted with a series of concentrations (100 fg/mL to 100 ng/mL) of $A\beta_{1\text{-}42}$ in PBS. (D) Transfer characteristics and (E) the shift of V_{Dirac} measured when the Tau-5-immobilized gFET was exposed to t-Tau (concentration: 100 fg/mL to 100 ng/mL). Dashed line represents the 3-fold noise level (~9.78 mV) from the blank control test. (C) Selectivity of the gFET biosensor toward pivotal AD biomarkers and non-specific proteins and their mixture. The $|\Delta V_{Dirac}|$ values of Aβ+Tau show the results of multiplexed detection of $A\beta_{1\text{-}42}$ and t-Tau. Aβ+BDNF and Tau+α-syn indicate the results after incubation of a mixture of proteins possessing opposite charges. The concentrations of $A\beta_{1\text{-}42}$, t-Tau, α-synuclein, and BDNF were same and equal to 10 pg/mL. Error bars correspond to standard deviations (n = 3).

and α-syn) were almost negligible. Meanwhile, when $A\beta_{1\text{-}42}$ was introduced, V_{Dirac} shifted to the left, indicating that $A\beta_{1\text{-}42}$ was specifically bound to 6E10 antibodies and n-doping occurred. The $|\Delta V_{Dirac}|$ of BDNF, t-Tau, and α-syn were 4.33 ± 2.10 mV, 5.12 ± 3.41 mV, and 3.89 ± 1.42 mV, respectively. On the other hand, the ΔV_{Dirac} of 10 pg/mL $A\beta_{1\text{-}42}$, the specific antigen, was measured as 38.79 ± 4.77 mV. Similarly, in Fig. S5D, the transfer curves obtained from sequential reactions with 10 pg/mL of α-syn, $A\beta_{1\text{-}42}$, BDNF, and t-Tau on Tau-5-immobilized gFET are shown. During non-specific target incubations, V_{Dirac} barely shifted. The $|\Delta V_{Dirac}|$ of α-syn, $A\beta_{1\text{-}42}$, and BDNF were found to be 4.33 ± 2.10 mV, 5.12 ± 3.41 mV, and 3.89 ± 1.42 mV, respectively. However, $|\Delta V_{Dirac}|$ of 10 pg/mL t-Tau was 77.29 ± 5.12 mV on Tau-5-immobilized biosensors.

To further explore the specificity of the gFET biosensor, a mixture with a non-specific protein having electrical charges that are opposite those of the specific target was injected to both 6E10-immobilized and Tau-5-immobilized gFETs. Since BNDF has a positive charge at pH 7.4, it is expected that BDNF may act as a severe noise to accurate detection when the mixture of $A\beta_{1\text{-}42}$ and BDNF reacts with 6E10-immobilized biosensors. In Fig. S5B, the serial incubations of 10 pg/mL α-syn, 10 pg/mL t-Tau, and the mixture solution (10 pg/mL $A\beta_{1\text{-}42}$ + 10 pg/mL BDNF) are shown. There was no significant shift in the transfer curves as a result of α-syn and t-Tau, as verified previously. When the mixture of $A\beta_{1\text{-}42}$ and BDNF was introduced, n-type doping occurred on the gFET with ΔV_{Dirac} value of −32.5 ± 4.1 mV. This is a slightly lower change than the value obtained when 10 pg/mL $A\beta_{1\text{-}42}$ reacted alone (−38.79 ± 4.77 mV); however, good detection performance was confirmed even in the reaction with a mixture of proteins and different charges. Similarly, α-syn is considered an electrical hindrance protein to the specific detection of t-Tau in Tau-5-immobilized gFETs. In Fig. S5E, the serial incubation of 10 pg/mL $A\beta_{1\text{-}42}$, BDNF, and the mixture solution (10 pg/mL t-Tau + 10 pg/mL α-syn) are shown. The ΔV_{Dirac} values of $A\beta_{1\text{-}42}$ and BDNF were also almost negligible. The ΔV_{Dirac} of the mixture (t-Tau + α-syn) solution reached 61.23 ± 8.21 mV, which is comparable to the ΔV_{Dirac} value of specific detection of 10 pg/mL of t-Tau alone.

To confirm the capabilities of multiplexed detection of $A\beta_{1\text{-}42}$ and t-Tau on gFET sensor array, we immobilized both 6E10 antibody and Tau-5 antibody on rGO array devices. We introduced 10 pg/mL of α-syn, BDNF, and mixture solution (10 pg/mL $A\beta_{1\text{-}42}$ + 10 pg/mL t-Tau) on these devices, and observed no significant response for non-specific analytes (α-syn and BDNF). In contrast, when a mixture of $A\beta_{1\text{-}42}$ and t-Tau was injected into a gFET array, significant changes in V_{Dirac} were observed only in the gFETs in which their specific antibodies were immobilized. As shown in Figs. S5C and S5F, our gFET devices can completely discriminate the targets even in the mixture of AD biomarkers (10 pg/mL $A\beta_{1\text{-}42}$ + 10 pg/mL t-Tau), comparable to the single detection of each AD biomarkers. The results obtained from the mixed biomarkers reactivity test and multiplexed detection, as well as non-specific target detections are shown in Fig. 4C and F. These results confirm the high specificity of our gFET and the capability of

multiplexed detection of AD biomarkers.

3.4. Specific detection in aCSF and human plasma

We validated the detection of $A\beta_{1\text{-}42}$ and t-Tau in biofluids to investigate the clinical applicability of the gFET. Different concentrations of $A\beta_{1\text{-}42}$ and t-Tau ranging from 100 fg/mL to 100 ng/mL were spiked into aCSF and diluted human plasma. Diluted human plasma was prepared by mixing at a ratio of 1:10 in 10 mM PBS buffer (pH 7.4). The responses to $A\beta_{1\text{-}42}$ and t-Tau exhibited the same proclivity of transfer curve shifts as that obtained in PBS buffer-based detections. In Fig. 5A and B, the transfer curves of the gFET at varying concentrations of $A\beta_{1\text{-}42}$ and t-Tau in aCSF, respectively, are shown. As the concentration of $A\beta_{1\text{-}42}$ increased from 100 fg/mL to 100 ng/mL, ΔV_{Dirac} of gFETs were measured to be -28.20 ± 9.91 mV, -53.55 ± 10.88 mV, -70.81 ± 8.84 mV, -90.27 ± 6.57 mV, -104.28 ± 3.58 mV, -119.62 ± 2.08 mV, and -134.73 ± 10.52 mV. The corresponding shift of the V_{Dirac} transfer curves is shown in Fig. 5C. A regression equation of the response was obtained as $\Delta V_{Dirac} = -17.33 \log C - 51.26$, with a correlation coefficient (R^2) of 0.991, where C is the $A\beta_{1\text{-}42}$ concentration. In addition, with the increase in t-Tau concentration from 100 fg/mL to 100 ng/mL, the ΔV_{Dirac} values of gFETs were 13.31 ± 2.70 mV, 30.29 ± 7.51 mV, 43.24 ± 8.51 mV, 62.42 ± 2.06 mV, 90.32 ± 7.35 mV, 106.22 ± 6.30 mV, and 126.43 ± 7.74 mV. The linear dependence of ΔV_{Dirac} on the logarithmic concentrations of t-Tau was also determined ($R^2 = 0.992$) within the clinically relevant range of 100 fg/mL to 100 ng/mL (Hansson et al., 2019). In Fig. 5D, the regression equation is $\Delta V_{Dirac} = 19.22 \log C - 29.01$.

We investigated the accuracy of the gFET array by detecting $A\beta_{1\text{-}42}$ and t-Tau spiked in diluted human plasma. The transfer curves of gFET at varying concentrations of $A\beta_{1\text{-}42}$ and t-Tau spiked in human plasma, respectively, are depicted in Fig. 6A and D. The ΔV_{Dirac} values of gFETs with serial interaction at varying concentrations from 100 fg/mL to 100 ng/mL $A\beta_{1\text{-}42}$ were -10.54 ± 6.99 mV, -26.41 ± 2.97 mV, -38.63 ± 3.54 mV, -51.76 ± 1.75 mV, -59.69 ± 2.64 mV, -69.00 ± 4.58 mV, and -72.78 ± 3.05 mV (Fig. 6B). The reactivity of $A\beta_{1\text{-}42}$ spiked in human plasma was slightly lower than that of PBS or aCSF, which is considered to be result of numerous non-target proteins contained in human plasma. Nevertheless, a linear relationship exists within the clinically relevant concentration range and a low LOD of 1 pg/mL (Mehta et al., 2000). Considering that the molecular weight of $A\beta_{1\text{-}42}$ is 4.5 kDa, its LOD is 222 fM, which is 10–100 times lower than the concentration of $A\beta_{1\text{-}42}$ in the blood of Alzheimer patients, as reported in the literature (Höglund et al., 2004). These results demonstrate sufficient possibilities for the application of gFETs to clinical plasma samples. In the case of t-Tau, as the concentration increased from 100 fg/mL to 100 ng/mL, the ΔV_{Dirac} values were 20.30 ± 1.78 mV, 38.55 ± 3.96 mV, 58.80 ± 6.15 mV, 73.70 ± 4.95 mV, 92.26 ± 4.30 mV, 106.38 ± 5.50 mV, and 112.02 ± 7.44 mV (Fig. 6E). Furthermore, there is no significant difference in the sensitivity in PBS or aCSF. A linear relationship also exists within a range that is clinically relevant (from 100 fg/mL to 10 ng/mL) (Zetterberg et al., 2013), and there were no significant differences in the sensitivity compared with that of PBS or aCSF. Considering that the molecular weight of t-Tau is 45.8 kDa, the LOD of t-Tau spiked in human plasma was estimated as 21.8 fM, which corresponds to 1 pg/mL. In Figs. 6C and 6F, ΔV_{Dirac} at various concentrations of $A\beta_{1\text{-}42}$ and t-Tau, respectively, are depicted. These results demonstrate that gFET can be applied to clinical samples with significantly good

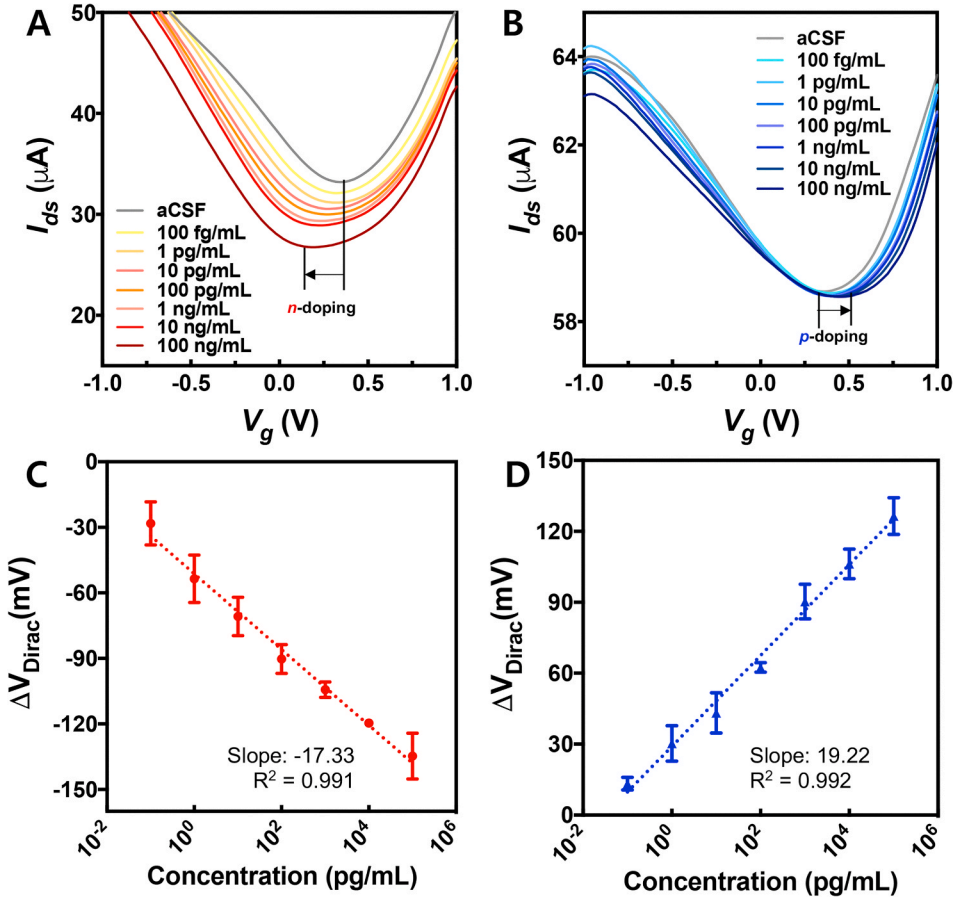

Fig. 5. (A) Transfer curves and (C) the shift of V_{Dirac} of the 6E10-immobilized gFET biosensor that interacted with increasing concentrations (100 fg/mL to 100 ng/mL) of $A\beta_{1\text{-}42}$ in aCSF. (B) Transfer curves and (D) the shift of V_{Dirac} of the gFET t-Tau for a series of concentrations (100 fg/mL to 100 ng/mL) in aCSF. Error bars correspond to standard deviations (n = 3).

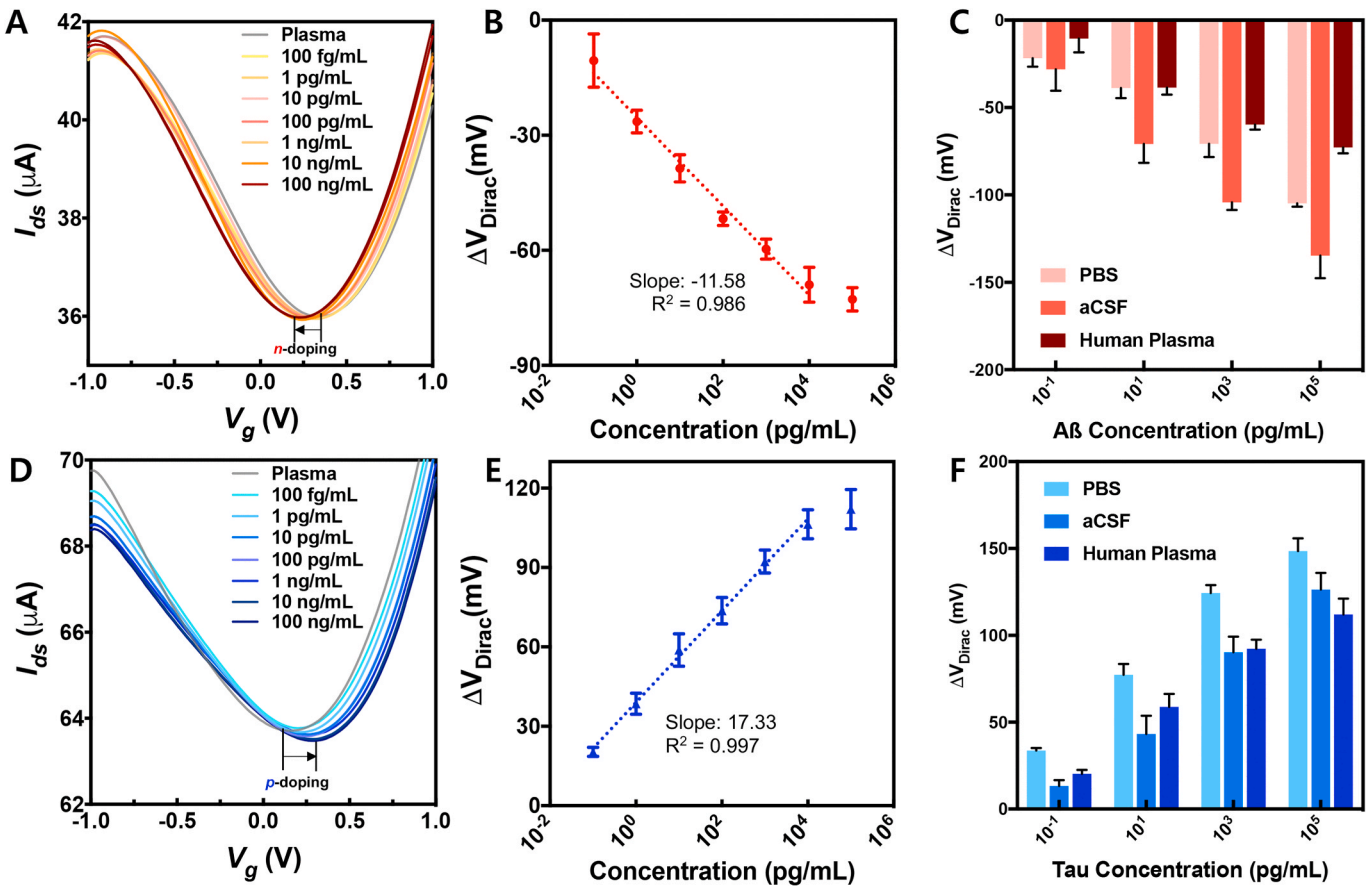

Fig. 6. (A) Transfer curves and (B) the shift of V_{Dirac} of the 6E10-immobilized gFET biosensor that interacted with increasing concentrations (100 fg/mL to 100 ng/mL) of $A\beta_{1\text{-}42}$ in human plasma. (D) Transfer curves and (E) the shift of V_{Dirac} of the Tau5-immobilized gFET biosensor that interacted with increasing concentrations (100 fg/mL to 100 ng/mL) of t-Tau in human plasma. (C) The ΔV_{Dirac} values after the 6E10-immobilized gFET biosensors were incubated with $A\beta_{1\text{-}42}$ in PBS, aCSF, and human plasma. (F) The ΔV_{Dirac} values after the Tau-5-immobilized gFET biosensors were incubated with t-Tau in PBS, aCSF, and human plasma. Error bars correspond to standard deviations (n = 3).

sensitivity in PBS, as well as in biofluids such as aCSF and human plasma.

4. Conclusions

In this study, we developed a label-free and highly sensitive gFET with simultaneous detection of multiple biomarkers of AD pathogenesis. The two major biomarkers of AD, $A\beta_{1\text{-}42}$ and t-Tau, caused shifts of V_{Dirac} in opposite directions based on their difference in pI, and a high sensitivity was achieved with femtomolar limit of detection of each biomarker. Several studies have successfully detected biomarkers using pI or the charge of the analyte on gFET; however, this is the first study to perform multiplexed detection using the difference between the pI values of two highly related biomarkers of the disease. In addition, we performed simultaneous detection of $A\beta_{1\text{-}42}$ and t-Tau with high specificity in a mixture of biomarkers of degenerative neurological diseases with different charges in physiological conditions. We also detected these two major biomarkers with high specificity and sensitivity in aCSF and human serum. It is expected that our gFET platform can be successfully applied to clinical practice as several studies have recently demonstrated that combined factors (e.g. $A\beta_{1\text{-}42}$/t-Tau and $A\beta_{1\text{-}42}$/phosphorylated-tau) derived from multiplexed detection can be used to propose a more accurate method for early diagnosis of AD compared to the detection of single biomarkers.

CRediT authorship contribution statement

Dongsung Park: Conceived The Idea, Designed Experiments, Performed Most Of Experiments, Formal analysis, And Manuscript Writing, Discussed The Results And Commented On The Manuscript. **Jae Hyun Kim:** Conceptualization, The Idea, Designed Experiments, Performed Most Of Experiments, Formal analysis, And Manuscript Writing, Discussed The Results And Commented On The Manuscript. **Hye Jin Kim:** Conceptualization, The Idea, Designed Experiments, Discussed The Results And Commented On The Manuscript. **Dongtak Lee:** Discussed The Results And Commented On The Manuscript. **David S. Lee:** Discussed The Results And Commented On The Manuscript. **Dae Sung Yoon:** Conceptualization, The Idea, Designed And Supervised The Study, Formal analysis, And Wrote The Manuscript, Discussed The Results And Commented On The Manuscript. **Kyo Seon Hwang:** Conceptualization, The Idea, Designed And Supervised The Study, Formal analysis, And Wrote The Manuscript, Discussed The Results And Commented On The Manuscript, Designed Experiments.

Declaration of competing interest

The authors declare no competing financial interests.

Acknowledgements

This work was supported by a grant from Kyung Hee University in 2019 (KHU-20192440).

Appendix A. Supplementary data

Supplementary data to this article can be found online at https://doi.org/10.1016/j.bios.2020.112505.

References

Carrico, Z.M., Le, G., Malinow, R., 2017. J. Biol. Methods 4, 77.
Chae, M., Kyoung, Y., Kim, J., Geun, T., Seon, K., 2018. Sensor. Actuator. B Chem. 272, 448–458.
Chen, T. Bin, Lee, Y.J., Lin, S.Y., Chen, J.P., Hu, C.J., Wang, P.N., Cheng, I.H., 2019. Sci. Rep. 9, 1–10.
Chen, X., Liu, Y., Fang, X., Li, Z., Pu, H., Chang, J., Chen, J., Mao, S., 2019. 126, 664–671..
Fu, W., Jiang, L., van Geest, E.P., Lima, L.M.C., Schneider, G.F., 2017. Adv. Mater. 29, 1–25.
Hansson, O., Lehmann, S., Otto, M., Zetterberg, H., Lewczuk, P., 2019. Alzheimer's Res. Ther. 11, 1–15.
Hao, Z., Zhu, Y., Wang, X., Rotti, P.G., Dimarco, C., Tyler, S.R., Zhao, X., Engelhardt, J.F., Hone, J., Lin, Q., 2017. ACS Appl. Mater. Interfaces 9, 27504–27511.
Hassan, Q., Kerman, K., 2019. Curr. Opin. Electrochem. 14, 89–95.
Hempstead, B.L., 2015. Trans. Am. Clin. Climatol. Assoc. 126, 9–19.
Höglund, K., Wiklund, O., Vanderstichele, H., Eikenberg, O., Vanmechelen, E., Blennow, K., 2004. Arch. Plus 61, 333–337.
Janas, Teresa, Sapoń, K., Stowell, M.H.B., Janas, Tadeusz, 2019. Int. J. Mol. Sci. 20, 1–16.
Janelidze, S., Stomrud, E., Smith, R., Palmqvist, S., Mattsson, N., Airey, D.C., Proctor, N. K., Chai, X., Shcherbinin, S., Sims, J.R., Triana-Baltzer, G., Theunis, C., Slemmon, R., Mercken, M., Kolb, H., Dage, J.L., Hansson, O., 2020. Nat. Commun. 11, 1683.
Jin, X., Zhang, H., Li, Y.T., Xiao, M.M., Zhang, Z.L., Pang, D.W., Wong, G., Zhang, Z.Y., Zhang, G.J., 2019. Microchim. Acta 186, 223.
Kaisti, M., 2017. Biosens. Bioelectron. 98, 437–448.
Kim, D.J., Park, H.C., Sohn, I.Y., Jung, J.H., Yoon, O.J., Park, J.S., Yoon, M.Y., Lee, N.E., 2013. Small 9, 3352–3360.
Lee, J.C., Kim, S.J., Hong, S., Kim, Y.S., 2019. Exp. Mol. Med. 51, 53.
Lei, Y.M., Xiao, M.M., Li, Y.T., Xu, L., Zhang, H., Zhang, Z.Y., Zhang, G.J., 2017. Biosens. Bioelectron. 91, 1–7.
Mehta, P.D., Pirttilä, T., Mehta, S.P., Sersen, E.A., Aisen, P.S., Wisniewski, H.M., 2000. Arch. Neurol. 57, 100–105.
Mor, D.E., Ugras, S.E., Daniels, M.J., Ischiropoulos, H., 2016. Neurobiol. Dis. 88, 66–74.
Nakatsuka, N., Yang, K., Abendroth, J.M., Cheung, K.M., Xu, X., Yang, H., Zhao, C., Zhu, B., Rim, Y.S., Yang, Y., Weiss, P.S., Andrews, A.M., 2018. 324, 319–324..
Ngoc Le, H.T., Park, J., Chinnadayyala, S.R., Cho, S., 2019. Biosens. Bioelectron. 144, 111694.
Nisbet, R.M., Polanco, J.C., Ittner, L.M., Götz, J., 2015. Acta Neuropathol. 129, 207–220.
Park, J.C., Han, S.H., Yi, D., Byun, M.S., Lee, J.H., Jang, S., Ko, K., Jeon, S.Y., Lee, Y.S., Kim, Y.K., Lee, D.Y., Mook-Jung, I., 2019. Brain 142, 771–786.
Parnetti, L., Gaetani, L., Eusebi, P., Paciotti, S., Hansson, O., El-Agnaf, O., Mollenhauer, B., Blennow, K., Calabresi, P., 2019. Lancet Neurol. 18, 573–586.
Pillai, J.A., Bonner-Jackson, A., Bekris, L.M., Safar, J., Bena, J., Leverenz, J.B., 2019. J. Alzheim. Dis. 70, 1051–1058.
Shahnawaz, M., Mukherjee, A., Pritzkow, S., Mendez, N., Rabadia, P., Liu, X., Hu, B., Schmeichel, A., Singer, W., Wu, G., Tsai, A.L., Shirani, H., Nilsson, K.P.R., Low, P.A., Soto, C., 2020. Nature 578, 273–277.
Song, F., Poljak, A., Valenzuela, M., Mayeux, R., Smythe, G.A., Sachdev, P.S., 2011. J. Alzheim. Dis. 26, 365–375.
Sügis, E., Dauvillier, J., Leontjeva, A., Adler, P., Hindie, V., Moncion, T., Collura, V., Daudin, R., Loe-Mie, Y., Herault, Y., Lambert, J.C., Hermjakob, H., Pupko, T., Rain, J.C., Xenarios, I., Vilo, J., Simonneau, M., Peterson, H., 2019. Sci. data 6, 151.
Tsai, S.J., 2003. Brain-derived neurotrophic factor: Med. Hypotheses 61, 110–113.
Verwey, N.A., Veerhuis, R., Twaalfhoven, H.A.M., Wouters, D., Hoozemans, J.J.M., Bollen, Y.J.M., Killestein, J., Bibl, M., Wiltfang, J., Hack, C.E., Scheltens, P., Blankenstein, M.A., 2009. J. Immunol. Methods 348, 57–66.
Weickert, S., Wawrzyniuk, M., John, L.H., Rüdiger, S.G.D., Drescher, M., 2020. Sci. Adv. 6 eaax6999.
Wu, D., Yu, Y., Jin, D., Xiao, M.M., Zhang, Z.Y., Zhang, G.J., 2020. Anal. Chem. 92, 4006–4015.
Yoo, Y.K., Kim, G., Park, D., Kim, J., Kim, Y.S., Yun Kim, H., Yang, S.H., Lee, J.H., Hwang, K.S., 2020. Sensor. Actuator. B Chem. 308, 127710.
Yu, Y., Li, Y.T., Jin, D., Yang, F., Wu, D., Xiao, M.M., Zhang, H., Zhang, Z.Y., Zhang, G.J., 2019. Anal. Chem. 91, 10679–10686.
Yue, W., Tang, C., Wang, C., Bai, C., Liu, S., Xie, X., Hua, H., Zhang, Z., Li, D., 2017. RSC Adv. 7, 44559–44567.
Zetterberg, H., Wilson, D., Andreasson, U., Minthon, L., Blennow, K., Randall, J., Hansson, O., 2013. Alzheimer's Res. Ther. 5, 4–6.
Zhang, C., Xu, J.Q., Li, Y.T., Huang, L., Pang, D.W., Ning, Y., Huang, W.H., Zhang, Z., Zhang, G.J., 2016. Anal. Chem. 88, 4048–4054.